[Geophysical Research Letters]

Supporting Information for

Greenland Ice Sheet ice slab expansion and thickening

N. Jullien[1], A. J. Tedstone[1], H. Machguth[1], N. B. Karlsson[2], V. Helm[3]

[1]Department of Geosciences, University of Fribourg, Fribourg, Switzerland

[2]Geological Survey of Denmark and Greenland, Copenhagen, Denmark

[3]Alfred Wegener Institute, Helmholtz Centre for Polar and Marine Sciences, Bremerhaven, Germany

Contents of this file

Introduction

In the following we provide additional information on the processing and interpretation of accumulation radar data in 2002-03 and 2010-18. We provide additional figures that are discussed in the main manuscript as well as in text S1, S2, S3 and S4.

Text S1. Ice content identification in 2002-2003

Dataset preparation

We downloaded all accumulation radar (AR) data acquired over the GrIS. We added coordinates to each radargram by matching the timestamps from the radargram with those provided in the flight path dataset. Radargrams were detrended in the logarithmic domain by the provider (J. Paden, personal communication 2020). We refer to the data in the radargrams as 'signal strength', in the unit of decibels.

Surface picking

We picked the ice sheet surface following the approach used by MacFerrin et al. (2019). First, we manually identified the surface at the start of each radargram. Then, for each trace in the radargram, the surface identification uses a vertical 100-pixel 3-standard deviation pseudo-Gaussian kernel mask over a 40 vertical pixels search window (150 vertical pixels search window in MacFerrin et al. (2019)), centered on the proposed surface. The identified surface of that trace corresponds to the index of the largest value from the convolution between the kernel mask and the radar signal in the search window. The index of the identified surface is then used as a suggested surface in the next trace, and so on until the end of the radargram is reached. When the algorithm failed to identify the surface then we picked the surface manually. The surface picking procedure was smoothed similarly to MacFerrin et al. (2019) by comparing the surface slope in each trace with the average surface slope of the 10 preceding traces. If the slope difference was larger than 5 vertical pixels or was 50% higher than the average slope of the 10 preceding traces, we considered the 20 traces ahead and found the trace whose slope is within 10% the mean slope of the 10 preceding traces. We then calculated the surface location by linear interpolation between the surface pixel before the jump and the next matching trace. We inspected all resulting surface picks manually.

As the firn column is considered to be dry during the springtime airborne radar campaigns, we used the speed of the electromagnetic signal through refrozen ice within firn derived by MacFerrin et al. (2019) to retrieve depth in each radargram. For further

details on the discussion of the speed of the electromagnetic signal in such a medium, we refer the reader to MacFerrin et al., (2019).

Ice content identification

We identified ice content via expert manual classification of the uppermost 30 m of each radargram. Each radargram was inspected using a histogram stretch between the 2.5% and 97.5% percentiles of the radar signal strength distribution from all the radargrams of the corresponding year. As these data have been detrended in the logarithmic domain we are limited to quantifying ice layer and slab extent only, leaving thickness estimates possible only occasionally.

Depending on the surface regime (i.e. ablation zone, percolation zone, dry snow zone), different characteristic features can be identified within the subsurface. Fig. 1 shows four radargrams (0-30 m) that represent different subsurface conditions. Radar returns in the ablation zone (Fig. 1b) are uniform with no major variations in signal strength. The percolation zone can show thin and sharp layering probably associated with decimeter-scale ice layers (Fig. 1c), but can also show meters-thick layering probably associated with ice slabs (Fig. 1d). The dry snow zone shows regular parallel layering associated with annual snow accumulation (Fig. 1e).

We considered whether the signal in Fig. 1c,d was indicative of ice content. Besides ice content, there are two other possibilities: (1) liquid water presence, and (2) wind-hardened, buried surface layers. To check the likelihood of these two other possibilities, we focus on a candidate radargram in SW Greenland (Fig. S1, similar to the one shown in Fig. 1d) where layers several meters thick are thought to correspond to ice. Liquid water was discounted as the return signal associated with liquid water shows typically a mirroring (peak on the opposite side) of the signal compared to the signal peak related to the surface (e.g. Fig. 18 in Karlsson et al. (2019)). This was not observed in the candidate radargram (Fig. S1b-e). Furthermore, liquid water would blind the radar signal below, but we do not see any evidence of this (Figs. 1d and S1b-e).

To investigate the possibility of a wind-hardened buried surface layer, we estimated the thickness of annual snowpack accumulation. Fettweis et al. (2020) indicate that mean annual snowfall ranges between 200 and 600 $\mathrm{mm\ w.e.\ year^{-1}}$ with a spread of 0-150 $\mathrm{mm\ w.e.\ year^{-1}}$ in the area of interest. This gives a low and high end of yearly snowfall of 50-750 $\mathrm{mm\ w.e.\ year^{-1}}$. Considering a firn density of 500 $\mathrm{kg \cdot m^{-3}}$ (Braithwaite et al., 1994) yields a plausible range of 0.1 to 1.5 m thickness for each buried surface layer. As the layers in the radargram are several meters thick it is therefore unlikely that the signal corresponds to a wind-hardened buried layer and so we conclude that the return signal is associated with ice slabs. We interpret thinner layers as indicative of ice layers (see thin layering in Fig. 1c).

Text S2. Ice content identification from 2010 to 2018

With radar data acquired during 2010 to 2018 we had two goals: first, to identify changing ice slab extent for comparison to the extents found in the 2002-03 period, and second, to quantify changes in slab thickness. This second goal required us to be able to quantitatively compare successive radargrams, necessitating a rigorous semi-automated approach to ice content identification.

Dataset preparation

We identified ice slabs in the L1B radargrams collected by the Accumulation Radar (AR) within NASA's Operation IceBridge following a similar approach to MacFerrin et al. (2019). We reprocessed the same 2010-2014 data as were used by MacFerrin et al. (2019). To identify ice slabs in data acquired during 2017 and 2018, we applied a location-based matching between the new radargrams and the 2010-2014 ice slabs extent found by MacFerrin et al. (2019). We retained all coincident radargrams as well as the ones in the vicinity of the ice slabs extent to ensure any changes in the subsurface firn near the pre-existing ice slabs would be identified. We applied a logarithmic transformation to the L1B radargrams (but did not multiply it by 10 as in Carl et al., (2011)) and refer to this as the 'signal strength' of the radargram, in the unit of decibels.

Surface picking and defining exclusions

From the log-transformed radargrams we picked the surface of the ice sheet following the approach used by MacFerrin et al. (2019) (Fig. S2a) . For 2017-2018 data, we manually identified the surface of the ice sheet at the start of each radargram and provided it to the algorithm. We then applied the surface pick to the radargram (Fig. S2b) and extracted the uppermost 100 m in order to carry out the corrections procedure outlined in the next step. We manually excluded areas with lakes and other obvious artefacts (i.e. signal failure) (Fig. S2c).

Correction for aircraft roll and signal attenuation with depth

We corrected the radar signal strength for the roll of the aircraft following MacFerrin et al. (2019) (Fig. S2d). On occasion, the roll correction failed, which was noticeable by

signal return strengths remaining much lower than following a successful roll correction. Such data were excluded from further analysis. In addition, much of the data collected in 2018 were affected by a periodicity artefact caused by the radar beam being steered off nadir during data collection (J. Li, personal communication, 2021) which prevented roll correction and made them ineligible for further analysis.

To ensure that radar signal strength returned from the subsurface would be comparable between radargrams, we subtracted the average surface radar signal strength from the sub-surface signal, thereby removing the majority of the atmospheric influences upon the return signal (Fig. S2e) while retaining the physical dimension of the radar signal. Finally, we corrected for depth attenuation of the radar signal following a slightly modified version from MacFerrin et al. (2019) (we did not apply variance normalisation) (Fig. S2f), and clipped each radargram to the uppermost 30 m corresponding to the depth range which is expected to contain ice slabs in order to simplify later processing steps.

Re-scaling of radar signal

Fourteen of the 448 radargrams (3%) displayed little variation in their return signal, making it difficult to identify ice slabs. We therefore rescaled these depth-corrected radargrams by applying a histogram stretch using the 5^{th} and 95^{th} percentiles from the combined distribution of the other depth-corrected radargrams.

Initial comparison with MacFerrin et al., (2019)

Initially, we reprocessed the 2010-14 data using the same ice identification algorithm as MacFerrin et al. (2019). They used a relative threshold unique to each radargram to identify ice slabs in the uppermost 20 m, but we found that this approach did not reliably return identical ice features between individual successive radargrams. Hence, the original algorithm is not well-suited to compare ice thickness across individual years. We therefore developed a new algorithm to identify ice slabs in the uppermost 20 m, based on the application of a universal range of radar signal strengths extracted from a reference radargram.

143 Identification of ice content versus porous firn

144 **Identifying the return signal strength that is indicative of ice content.** We aimed to
145 identify the range of radar signal strengths that enables differentiation between porous
146 firn versus ice content across the entire dataset. In 2013, MacFerrin et al. (2019) collected
147 in-situ ground penetrating radar data and firn cores coincident with an Operation
148 IceBridge AR radargram during the same spring, which they used to validate the
149 identification of ice slabs in airborne radar data. Here, we adopt this AR radargram as our
150 "reference radargram" (see Fig. S3a).

151 We manually identified ice slabs in the depth-corrected AR reference radargram (Fig.
152 S3b), referred as in-situ ice content. We adopted a conservative approach, seeking to
153 include ice which was positively identified in ground-based in-situ GPR data by
154 MacFerrin et al., (2019), easily distinguishable from porous firn, and continuous. Next, we
155 used this mask to extract the distributions of signal strength from the reference
156 radargram for (a) porous firn and (b) ice content (Fig. S4). The overlap in the signal return
157 strength between the two facies means that a single threshold to fully differentiate
158 porous firn and ice content cannot be defined. Instead, we developed an algorithm using
159 a range of thresholds based on the quantiles of the ice content signal distribution to
160 distinguish between ice content and porous firn.

161 Fig. S3c illustrates the performance of the new algorithm on the reference radargram in
162 detecting ice content for quantile 0.65 of the ice content distribution (our lower
163 threshold), and Fig. S3d for quantile 0.79 (our upper threshold). Quantile 0.65 is the
164 highest quantile for which the algorithm correctly identifies ice without erroneously
165 including firn (see Tab. S1), at the cost of missing some ice content (see Fig. S3c). Above
166 this threshold, some areas that have been mapped to be porous firn start to be falsely
167 identified as ice. These facies correspond to an intermediate state between porous firn
168 and ice slabs (see Fig. 2b,c in MacFerrin et al. (2019)), most likely several ice layers within
169 firn. By quantile 0.80 (not shown), porous firn unlikely to contain numerous ice layers
170 starts to be identified as ice. We therefore applied thresholds in the quantile range 0.65

to 0.79 from the ice content distribution to detect ice presence. We discuss accuracy further below.

Extracting ice content. For each radargram, we extracted ice content across the range of thresholds described above in 0.01 increments, corresponding to retrievals at 15 individual thresholds. Following MacFerrin et al. (2019), we removed small-scale noise by applying a filter to each ice content retrieval to remove small individual ice features 1-2 pixels wide, and a continuity threshold to retain only pixels which were spatially continuously connected to at least 350 other pixels. We show the resulting ice content identification for quantile 0.65 in Fig. S2h and quantile 0.79 in Fig. S2i. The ice features identified in each individual quantile is referred to ice slabs.

Ice content likelihood. We computed an ice content likelihood for each radargram as the percentage of the 15 different levels of ice content in which each pixel was identified as containing ice (Fig. S2g).

Post-processing and verification. In some radargrams we found that some porous firn areas were wrongly identified as ice, probably because of the significant overlap of the two distributions (Fig. S4). We therefore manually excluded these areas from the final results (Fig. S2j). The list of exclusions is provided in the code repository.

Accuracy assessment

We considered the accuracy of the extreme end members of the quantile range (quantile 0.65 and quantile 0.79). Tables S1 and S2 show the two contingency tables given by quantiles 0.65 and quantile 0.79 with respect to the in-situ ice content. As could be expected from the ice content and porous firn signal strength distributions (Fig. S4), a lower threshold quantile performs better in correctly identifying porous firn but performs less well in correctly identifying ice. Conversely, a higher threshold quantile performs better in identifying ice compared to a lower threshold but at the cost of a poorer performance in correctly identifying porous firn. Overall, the total accuracy is higher for the highest quantile.

Ice slab extent

As described in the main text, we defined ice slabs as present in areas with at least 1 m of subsurface ice content by the end of the study period. Following MacFerrin et al. (2019), we only mapped ice slabs above the long-term ELA (i.e. where firn exists), and so our lower ice slabs bounds match theirs.

Final comparison with MacFerrin et al. (2019)

At higher elevations, our ice slab identification yielded some differences with the identification by MacFerrin et al. (2019). Indeed, inspection of individual radargrams revealed that MacFerrin et al. (2019) incorrectly identified ice slabs in some areas, especially in the NE towards the high boundary. As a result, our final ice slab extent differs slightly from MacFerrin et al. (2019). The largest differences are found in the NW, NO and NE (Fig. S12). For example, our 2010-2018 upper ice slabs limit extends less inland compared to the 2010-2014 extent from MacFerrin et al., (2019) in-between upstream of Petermann glacier and Qaanaaq Mitarfik (Thule Air Base) in the NW and NO. The similar is observed upstream of Nioghalvfjerdsbrae (79 N Glacier) in the NE. Overall, MacFerrin et al., (2019) estimated ice slabs extended over 64’800-69’400 km^2 in 2014; we find ice slabs extended over 60’400-73’500 km^2 in 2018.

Text S3. Distinction between, 'in-initiation', 'in-development' and 'well-developed' ice slabs

We analyze the ice content change from the start to the end of the studied period. We identify three stages in ice slab development corresponding to their changes in thickness:

i. In the 'in-initiation' stage, the firn was free of ice slabs at the start of the studied period, and had developed new ice slabs by the end of the studied period.

ii. In the 'in-development' stage, ice slabs experienced substantial (metres) thickening during the studied period.

iii. In the 'well-developed' stage, the thickness of the ice slab was already large (i.e. larger than 10 m thick) at the start of the studied period; its thickness often increased further during the studied period.

In Fig. S5 we illustrate these different categories by splitting transect F (Fig. 3f) into corresponding sectors. Note that we did not set the maximum boundary of ice thickness to be 16m for this analysis; ice thickness can thus reach 20 m.

In the "well-developed" sector, the median ice content stayed roughly the same in 2017 compared to 2010 (14 m and 15 m respectively) (Fig. S5b), with negligible overall change (-2% in 2017 compared to 2010) (Fig. S5e).

In the "in-development" sector, the median ice content increased from 4.2 m to 11.5 m (Fig. S5c, see also the quantiles 0.25 and 0.75 in Table S3), equivalent to an increase of 194% from 2010 to 2017 (Fig. S5f).

In the "in-initiation" sector, no ice slab was identified in 2010, but a new ice slab had developed by 2017 (Fig. S5g) whose median ice content was 5 m in 2017 (Fig. S5d).

We performed the same analysis for transects C and D (Fig. 3c,d) and we present the results in Table S3. We conclude similar patterns as in transect F are taking place in transects C and D.

Text S4. Ice accretion

We differentiate between top-down ice accretion versus accretion on the undersides of ice slabs (Fig. 4d). From spring 2012 to spring 2018, both top-down and underside accretion took place, which is clearly identifiable once it has been separated from lateral and vertical displacement of the ice slab.

(i) **Lateral displacement:** Using local surface velocities measured from 2009 to 2013, we estimate that the ice was displaced laterally by ~312 m (Doyle et al., (2014)). This agrees well with the ~360 m that we estimate by comparing the distribution of ice content located between 15.93 and 16.52 km in 2012 with its corresponding location in 2018.

(ii) **Vertical displacement:** The bottom of the "double-layered" ice slab (from 13.8 to 15.6 km) in 2012 was found to be roughly 2.6 m lower by 2018, while the ice slab from 16.5 to 17.7 km was found 3m deeper (Fig. 4d). This apparent movement is due to subsequent accumulation. We estimated the burial of the ice slab bottom from 2012 to 2018 using ice cores collected previously (Rennermalm et al., (2021)). Due to extreme melting in summer 2012 (Fig. S6), the ice slab surface was exposed (Machguth et al., 2016), meaning that any firn pore space remaining from 2011-12 accumulation was minimal or non-existent. We were therefore able to estimate the lower boundary of the ice slab at KAN_U in 2013 and 2017, concluding that the bottom of the thick ice slab that developed in summer 2012 was buried by roughly 1.7 m from 2013 to 2017. We lack cores from 2018 and thus cannot estimate potential firn replenishment from spring 2017 to spring 2018. Nevertheless, this estimate of 1.7 m burial between 2013 and 2017 seems a reasonable lower bound approximation for 2012-2018 firn replenishment.

(iii) **Top-down accretion** took place on top of the slab, thickening the ice slab by 2.9 m from 2012 to 2018 in-between 16.5 and 17.7 km (Fig. 4d).

(iv) **Ice accretion on the undersides of ice slab** also occurred between 2012 and 2018 between 13.8 and 15.6 km, commencing at 11-13 m below the surface and extending to 20 m deep (Fig. 4d).

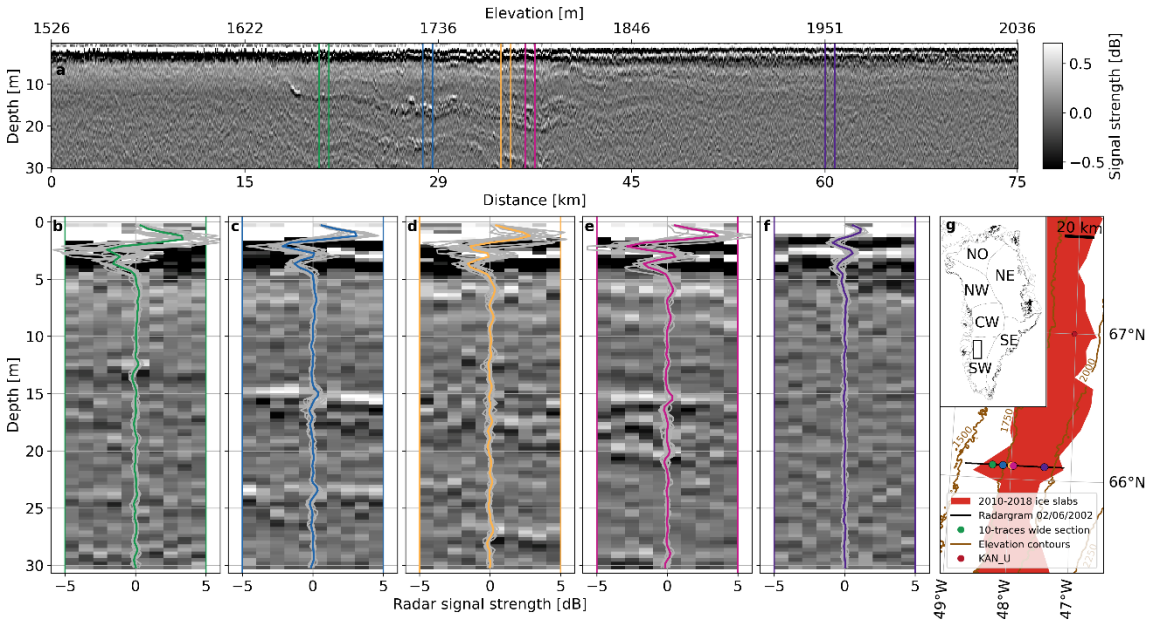

272

273 **Figure S1. Examples of ice content in 2003-03 data.** (a) Radargram acquired in SW
274 Greenland on June 2nd, 2002 (background) and 10-traces wide limits of radar signal
275 strength with color coding corresponding to panels b-f. (b-f) Individual trace signal
276 profile (grey lines), average over the 10 traces of interest (color), and 10-traces
277 radargram on the background. (b) An ice layer at 12-13 m depth. (c) Ice slabs are present
278 between 14 m and 17 m depth and between 23 m and 25 m depth, (d) between 10 m
279 and 20 m depth and at 27m depth, (e) in-between 15-21 m depth as well as at 29 m
280 depth. (f) Porous firn without ice layers nor slabs. (g) Location of radargram compared to
281 2010-2018 ice slabs extent.

282

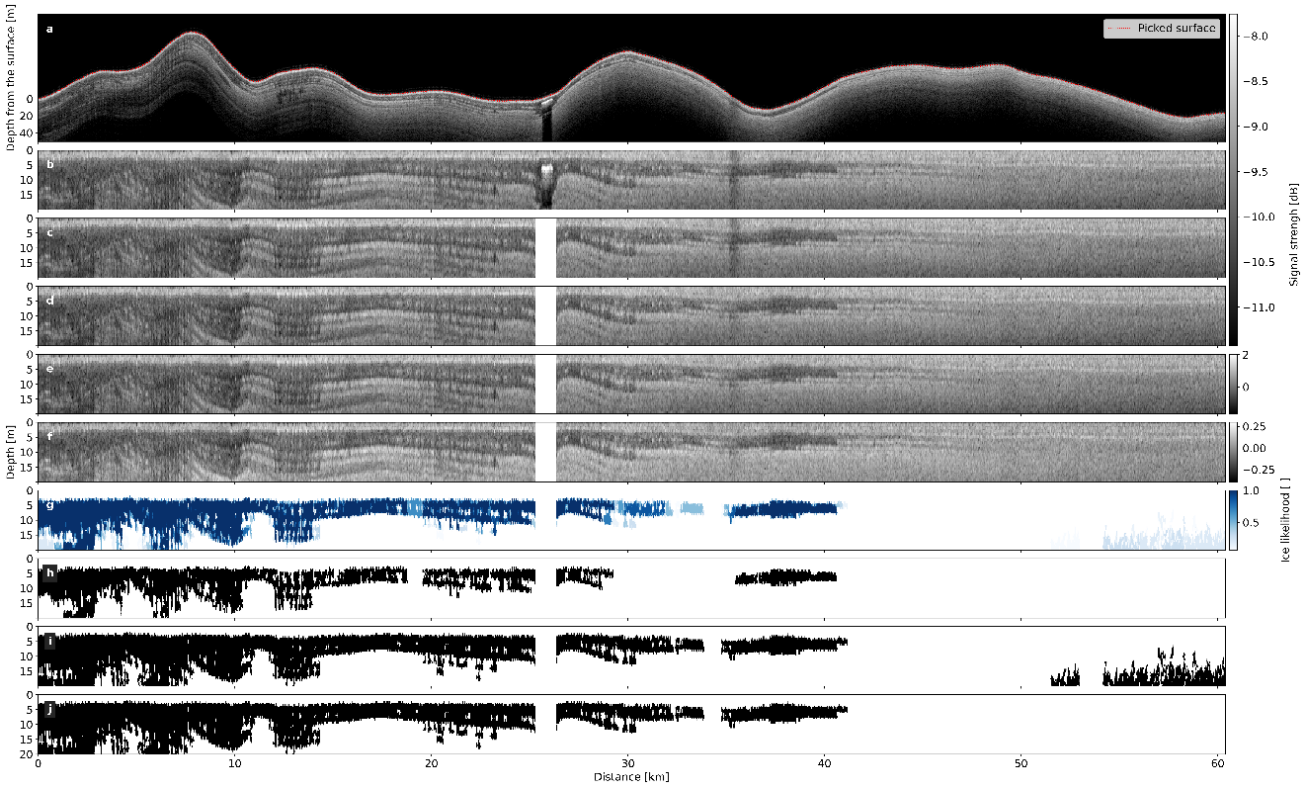

283

284 **Figure S2. Processing steps to identify ice content from airborne accumulation**
285 **radar data**, illustrated using radargram 20140416_05_007_009. (a) raw airborne
286 accumulation radar (AR) data before surface identification with the identified surface (red
287 dotted line). (b) AR data after surface picking. (c) AR data after screening for areas to be
288 excluded. (d) AR data after correction for the roll of the aircraft. (e) AR data after the
289 removal of the average surface signal strength. (f) AR data after correction for the
290 attenuation of the signal with depth. (g) Ice content likelihood, ranging from 0 to 1. (h)
291 Ice content presence where each cell was mapped as ice at quantile 0.65. (i) Ice content
292 presence where each cell was mapped as ice at quantile 0.79, corresponding to a
293 likelihood of 1. (j) Final ice content at quantile 0.79, following manual porous firn
294 exclusion.

295

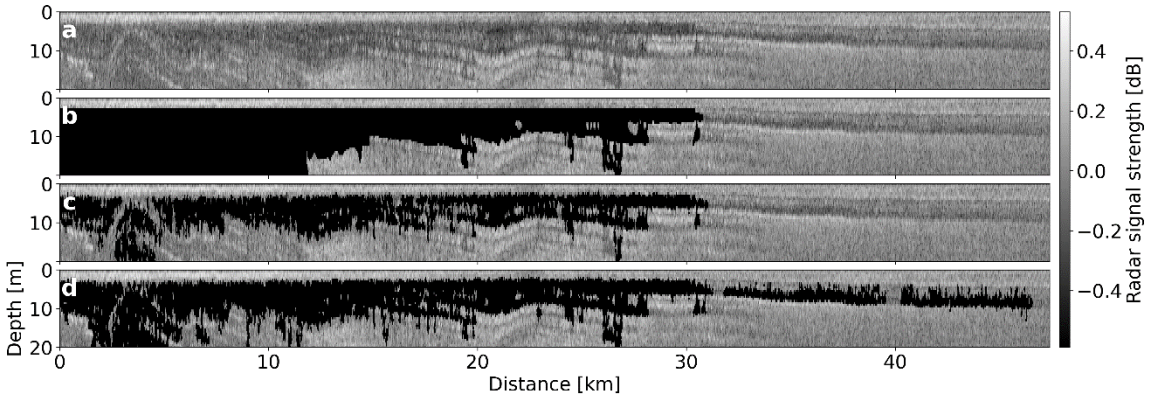

296

297 **Figure S3. Extraction of characteristic radar return strength from reference**
298 **radargram.** (a-d) Depth corrected data for the reference radargram derived from AR
299 data. (b) in-situ ice content mask (black). (c) Ice content retrieval using quantile 0.65 of
300 the ice content distribution signal strength derived by applying the in-situ ice content
301 mask (b) to the data in panel a. (d) As for panel c, using quantile 0.79.

302

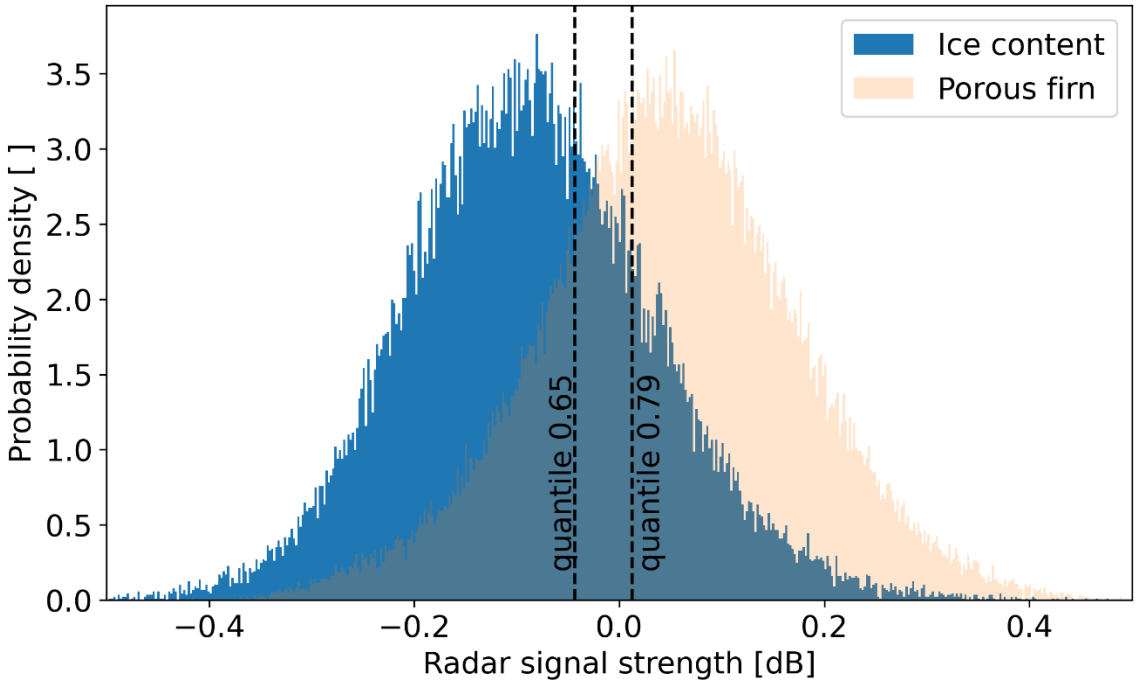

Figure S4. Porous firn versus ice content signal strength distribution. Calculated according to in-situ ice content in the depth-corrected reference radargram. The vertical dashed lines correspond to the quantile 0.65 and quantile 0.79 of the ice content distribution.

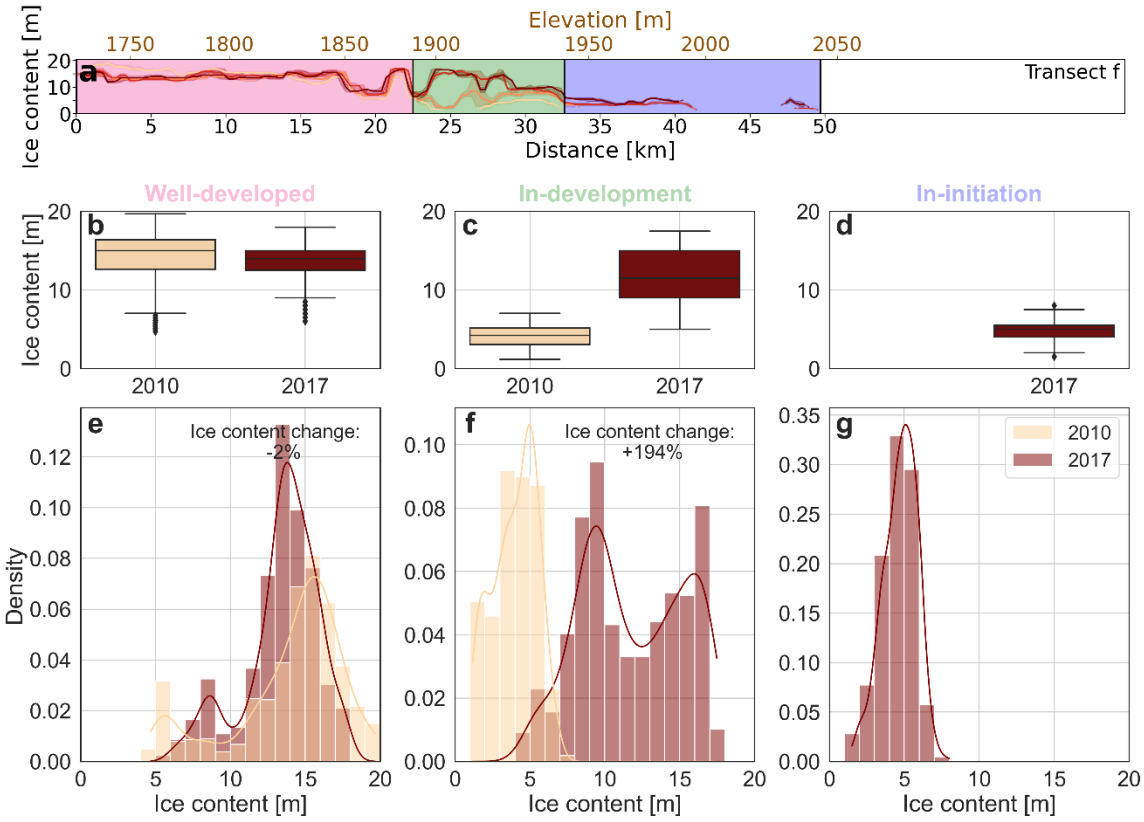

Figure S5. Ice content change along transect F. (a) Ice content change from 2010 to 2017 (colored lines, same as in Fig. 3f) along the transect. The different sectors of changes in ice slabs thickness are indicated by the background shading: well-developed (pink), in-development (green), in-initiation (blue). (b-d) Boxplot of ice content in 2010 and 2017 in the three sectors. (e-f) Distribution of ice content in 2010 and 2017 in the three sectors. Lines denotes the kernel density estimate of the distributions. Percentage change indicate the relative change in total ice content in the sector of interest in 2017 compared to 2010.

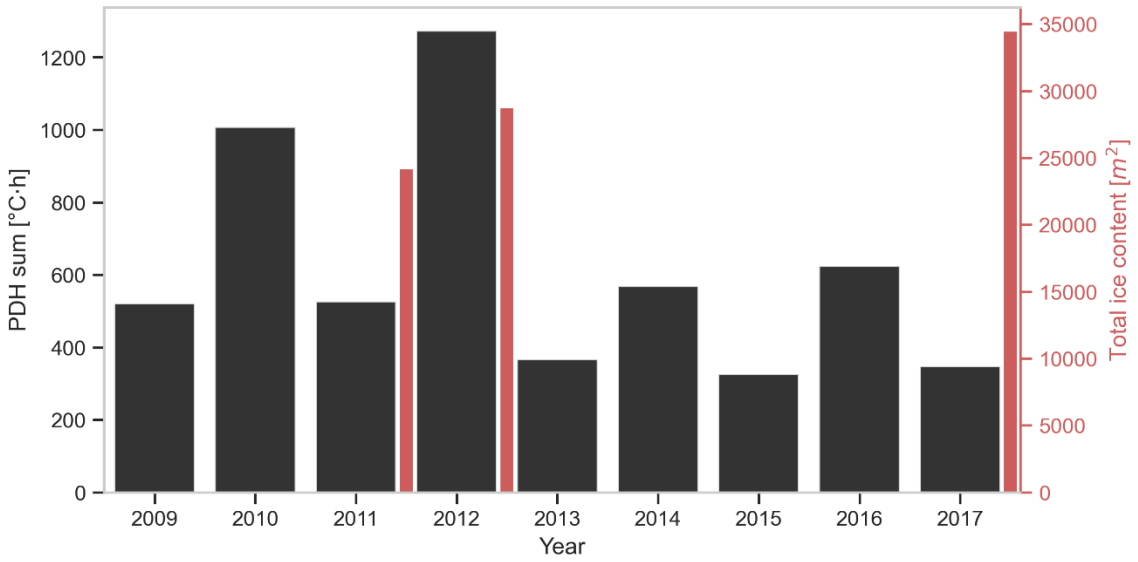

Figure S6. Melt potential at KAN_U. Positive Degree Hour sum [℃ · h] during each summer (black) and total ice content according to radargrams each spring (red) within the area delimited by thick dashed lines in Fig. 4 (from 13.8 to 17.7 km).

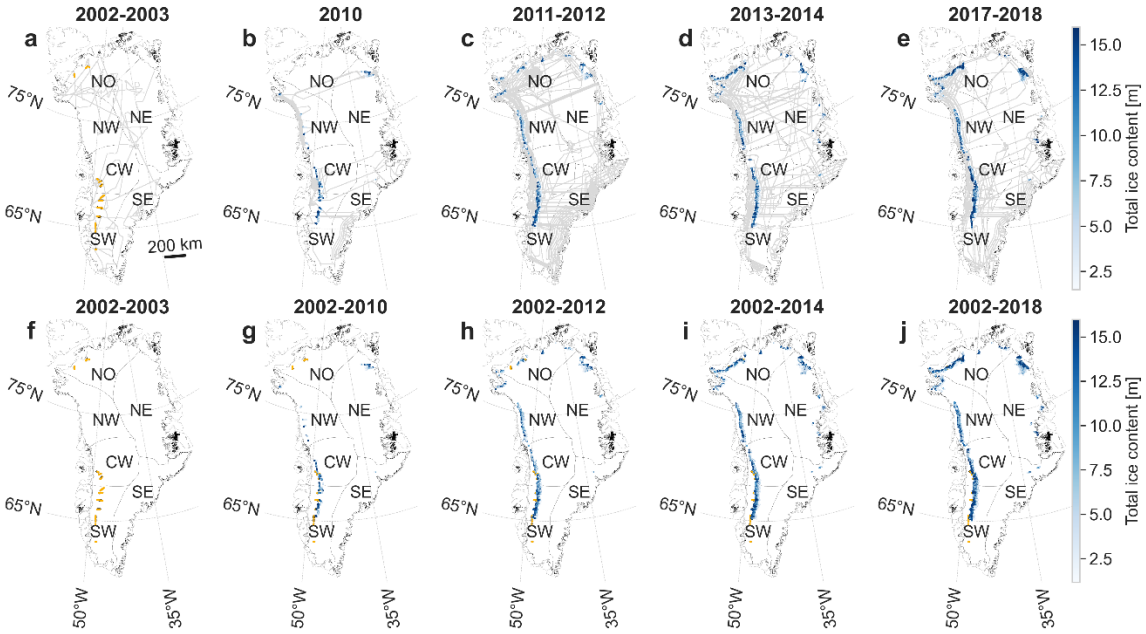

Figure S7. Ice slab mapping and growth over time. (a-e) Ice slabs mapped during each time period (color) and flight line (gray). (f-j) Cumulative ice slabs mapping (color) over successively longer time periods.

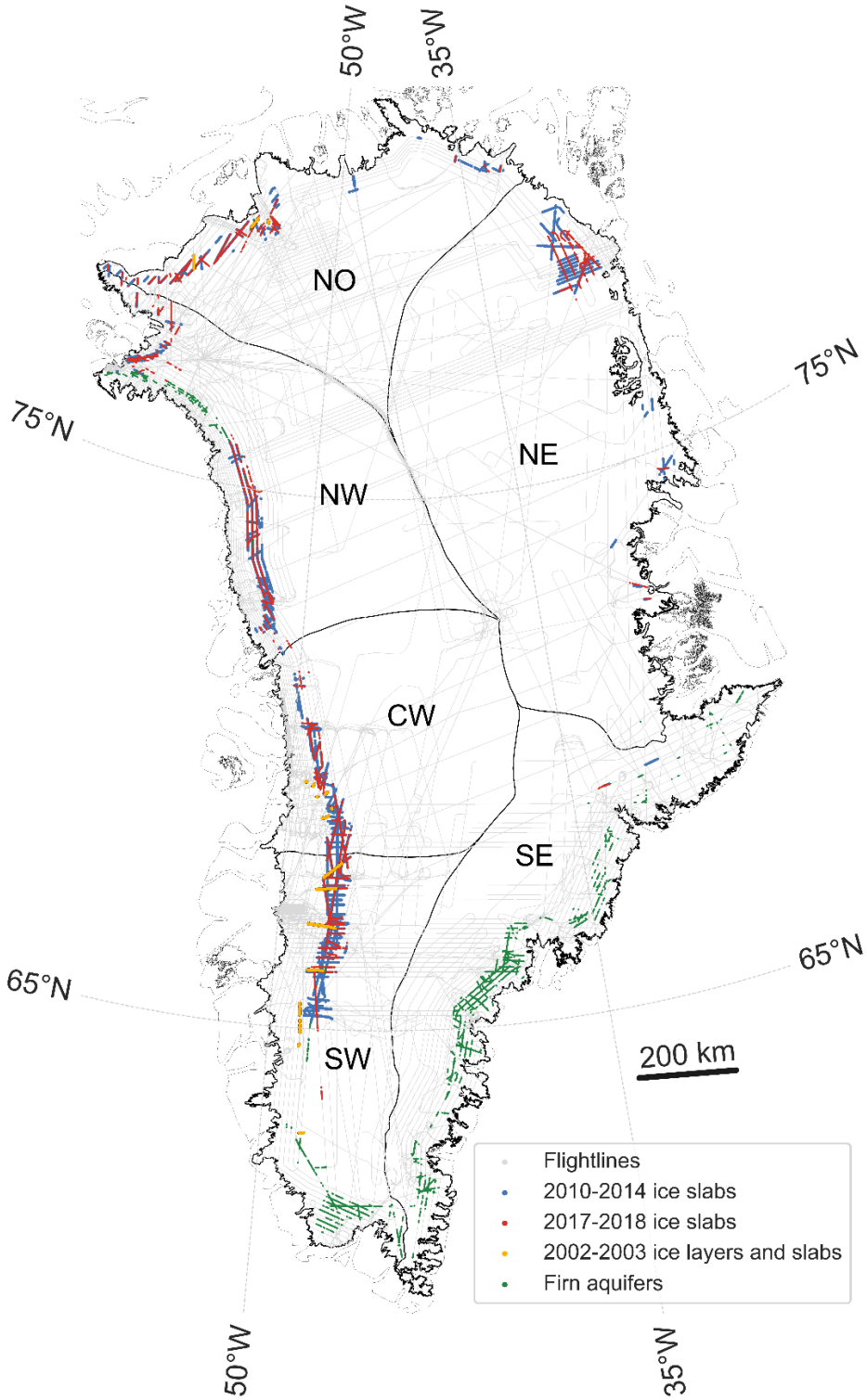

Figure S8. Combined ice slab presence from 2002 to 2018. Ice layers and slabs mapped in 2002-03 (orange), 2010-14 (blue) and 2017-18 (red), firn aquifers in 2010-2014 (Miège et al., 2016) (green). Flight lines associated with 2002-2018 ice slabs are displayed in the background in grey.

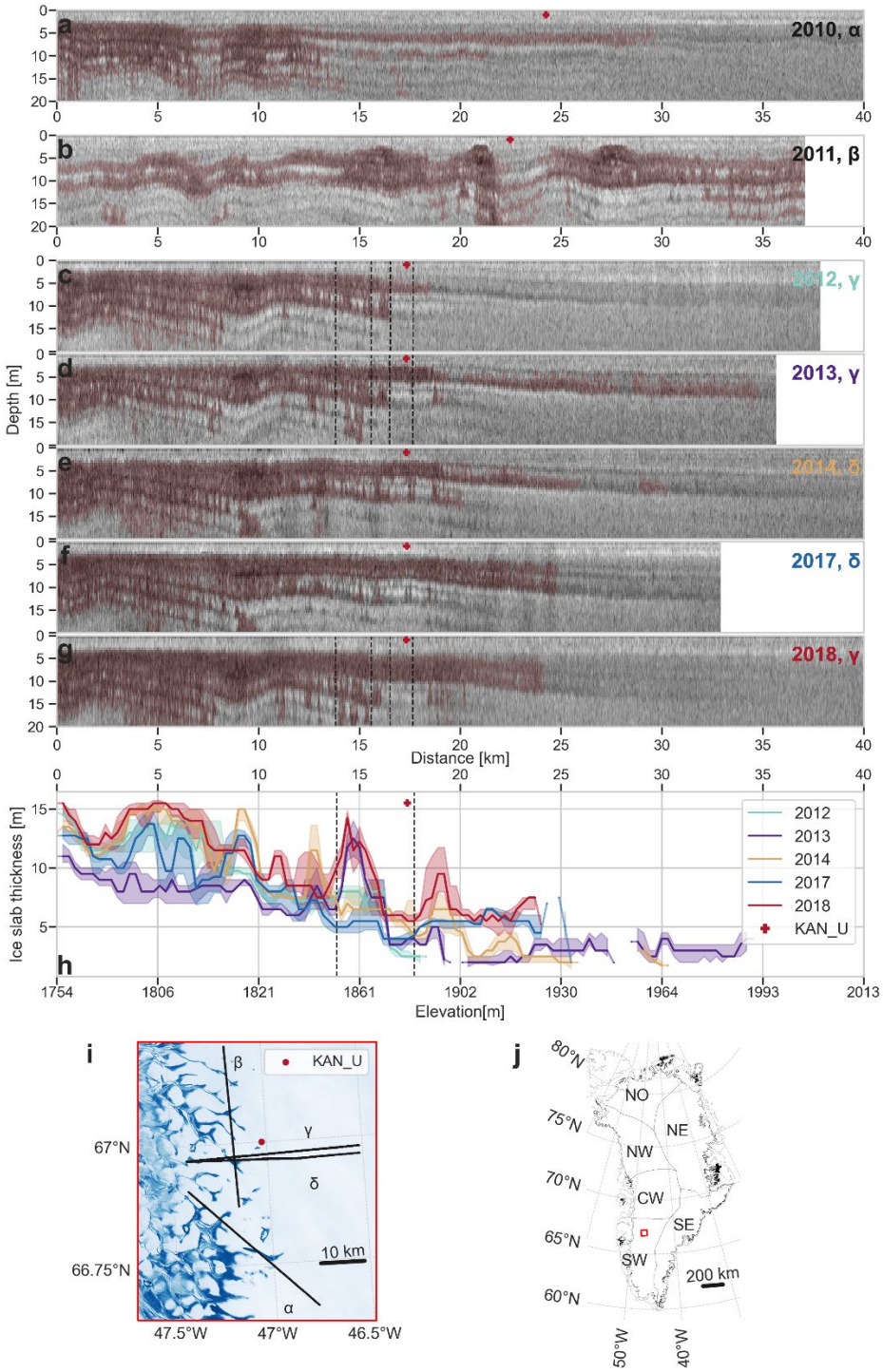

Figure S9. Ice thickness through time along a transect close to KAN_U (red marker in each panel). (a-g) Radargrams in greyscale and resulting maximum likely ice content (quantile 0.79) in red. Dashed vertical lines delineate the areas discussed in the text. (h) Ice slab thickness in uppermost 20 m of radargrams (from 2012 onwards). Equivalent elevation (m above WGS84 ellipsoid) on lower x axis. (i) Near-infrared (band 8) Sentinel-2 image acquired on August 23rd, 2021, with radargram locations. (j) Transect location on the GrIS (red square).

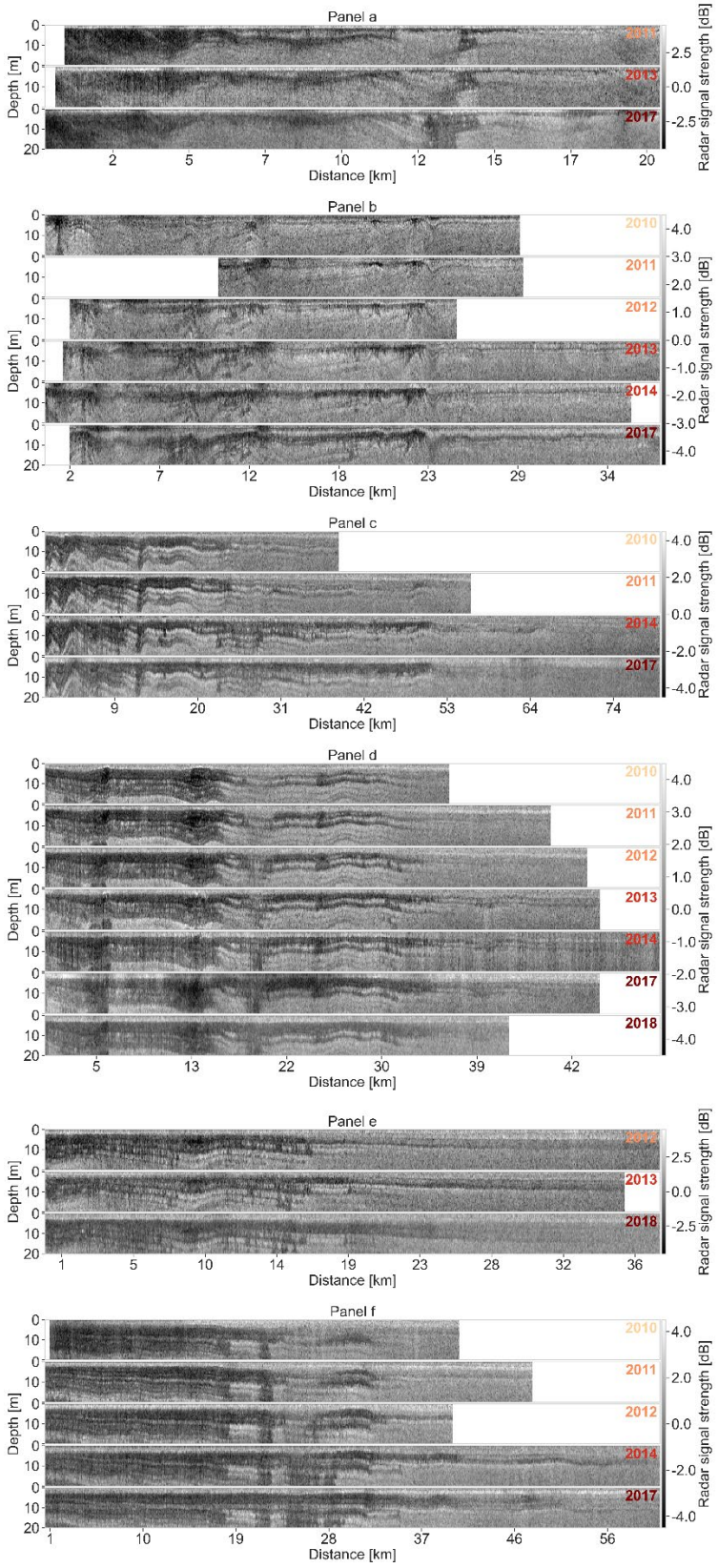

Figure S10. Yearly radargrams of transects used in Fig. 3

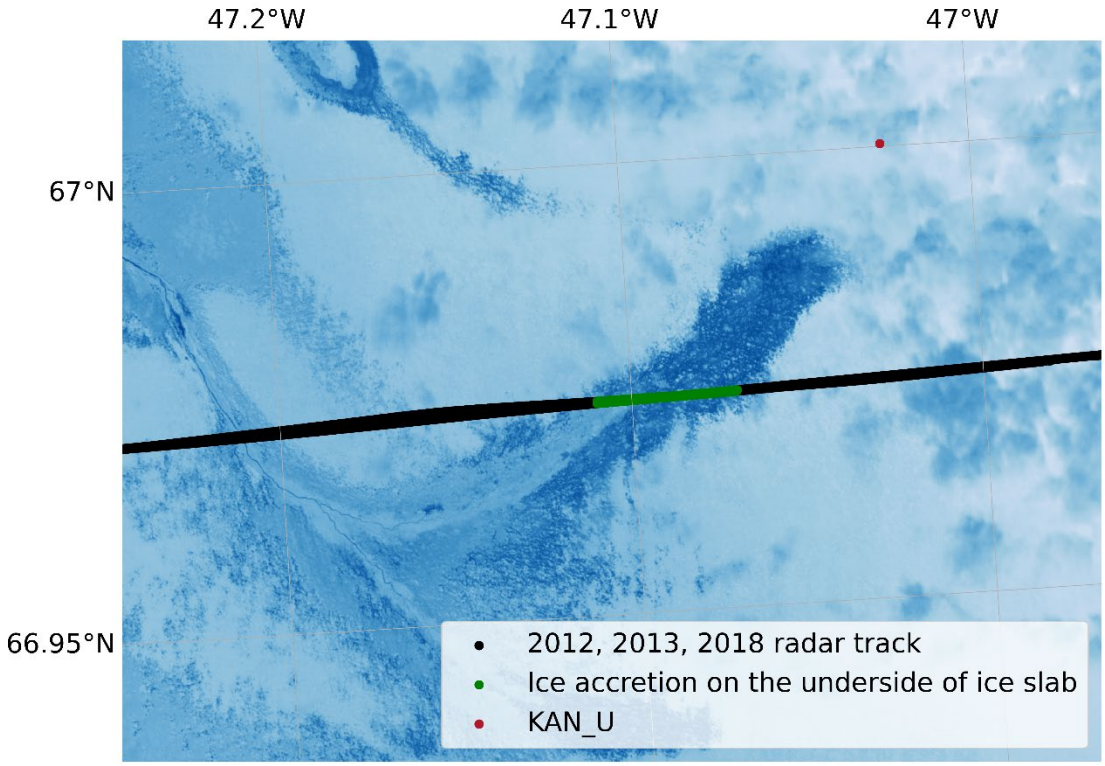

345

346 **Figure S11. Coincident surface hydrology and ice slab accretion.** Near-infrared (band
347 8) Sentinel-2 image acquired on August 24th, 2016. Dark blue corresponds to slush
348 fields. A developed hydrological network is seen in the lower left. Clouds are visible in
349 the upper right. Radargrams (black) acquired in 2012, 2013 and 2018 (same as Fig. 4b,d).
350 Radargrams with ice accretion on the underside of ice slab (green) identified by
351 comparing 2012 with 2013 and 2018 radargrams (13.8 to 15.6 km in Fig. 4). KAN_U is
352 indicated by the red dot.

353

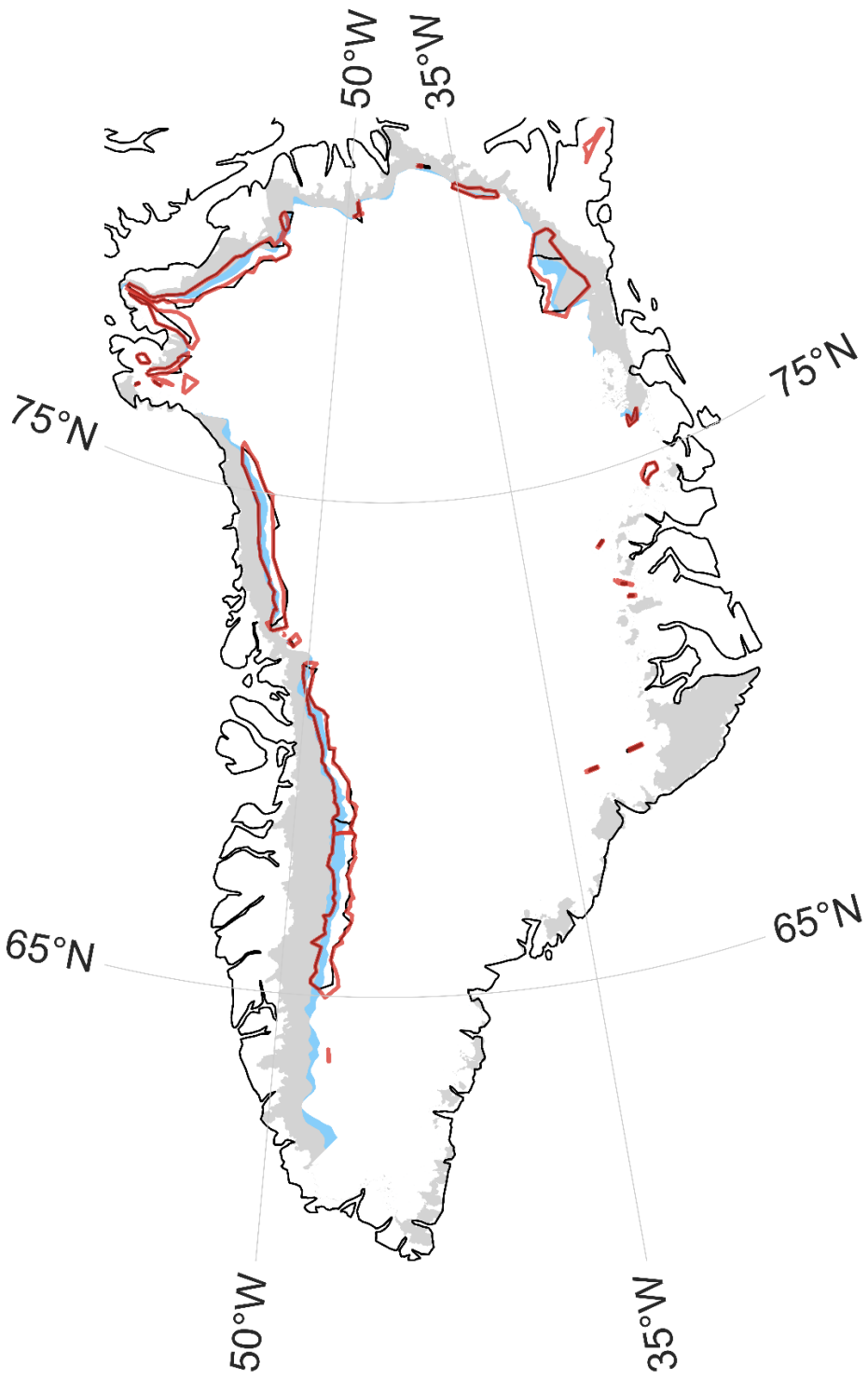

Figure S12. Comparison between visible surface runoff area and ice slab extent. Visible surface runoff area in 1985-1992 (grey shading) and expansion in 2013-2020 (blue shading) from Tedstone & Machguth (2022). Ice slabs extent in 2010-2014 from MacFerrin et al. (2019) (black). Ice slabs extent at quantile 0.79 in 2010-2018 in this study (red).

	Firn (Q 0.65)	Ice (Q 0.65)	Sum	Producer acc.
Firn (in situ)	**98894**	413	99307	99.58%
Ice (in situ)	19426	**21897**	41323	52.99%
Sum	118320	22310	**140630**	
User acc.	83.58%	98.15%		**Overall acc. 85.89%**

Table S1. Contingency table summarizing the performance of the algorithm in correctly retrieving porous firn and ice using quantile 0.65 of the ice content distribution as the threshold differentiating between porous firn and ice compared to the in-situ ice content being the reference. Values are in pixels. The producer's accuracy (producer acc.) relates to omission errors, e.g. not retrieving ice when it is ice, while the users' accuracy (user acc.) relates to commission errors, e.g. retrieving porous firn as ice. The overall accuracy (overall acc.) relates to how well the algorithm performs in correctly retrieving both ice and porous firn compared to the reference radargram.

	Firn (Q 0.79)	Ice (Q 0.79)	Sum	Producer acc.
Firn (in situ)	**92999**	6308	99307	93.65%
Ice (in situ)	11001	**30322**	41323	73.38%
Sum	104000	36630	**140630**	
User acc.	89.42%	82.78%		**Overall acc. 87.69%**

Table S2. As Table S1, using quantile 0.79 of the ice content distribution as the threshold.

	Year	Well-developed		In development		In initiation	
		[$Q_{0.25}$; $Q_{0.5}$; $Q_{0.75}$]	Change	[$Q_{0.25}$; $Q_{0.5}$; $Q_{0.75}$]	Change	[$Q_{0.25}$; $Q_{0.5}$; $Q_{0.75}$]	Change
C	2010	[7.7 ; 10.5 ; 13.6]	**+2%**	[3.7 ; 4.6 ; 5.1]	**+62%**	-	**-**
	2017	[6.0 ; 10.0 ; 15.0]		[5.0 ; 6.5 ; 8.5]		[4.5 ; 5.5 ; 6.0]	
D	2010	[11.5 ; 13.3 ; 15.5]	**+11%**	[2.6 ; 3.5 ; 4.4]	**+101%**	-	**-**
	2018	[12.5 ; 15.0 ; 16.5]		[5.0 ; 6.5 ; 9.0]		[4.5 ; 5.5 ; 6.0]	
F	2010	[12.6 ; 15.0 ; 16.4]	**-2%**	[3.0 ; 4.2 ; 5.1]	**+194%**	-	**-**
	2017	[12.5 ; 14.0 ; 15.0]		[9.0 ; 11.5 ; 15.0]		[4.0 ; 5.0 ; 5.5]	

Table S3. Summary statistics table of ice content on three transects in Fig. 3 (transects C, D, F), for the three stages of ice slab development at the start and end of the studied period. $Q_{0.25}$, $Q_{0.5}$, $Q_{0.75}$ correspond to quantiles 0.25, 0.5 and 0.75 of ice content respectively. The ice content change represents the relative change of ice content by 2017 compare to 2010.